

Hybrid additive manufacturing of 3D electronic systems

This content has been downloaded from IOPscience. Please scroll down to see the full text.

2016 J. Micromech. Microeng. 26 105005

(<http://iopscience.iop.org/0960-1317/26/10/105005>)

View [the table of contents for this issue](#), or go to the [journal homepage](#) for more

Download details:

IP Address: 207.162.240.147

This content was downloaded on 29/08/2016 at 18:38

Please note that [terms and conditions apply](#).

You may also be interested in:

[Organ Printing: Stereolithography-based 3D printing](#)

D-W Cho, J-S Lee, J Jang, J W Jung, J H Park and F Pati

[A facile method for integrating direct-write devices into three-dimensional printed parts](#)

Yung-Hang Chang, Kan Wang, Changsheng Wu et al.

[Laser 3D micro-manufacturing](#)

Alberto Piqué, Raymond C Y Auyeung, Heungsoo Kim et al.

[3D-printed bioanalytical devices](#)

Gregory W Bishop, Jennifer E Satterwhite-Warden, Karteek Kadimisetty et al.

[Inkjet deposited circuit components](#)

S M Bidoki, J Nouri and A A Heidari

[Fabrication methods and applications of microstructured gallium based liquid metal alloys](#)

M A H Khondoker and D Sameoto

[Flip-chip integration of Si bare dies on polymeric substrates at low temperature using ICA vias made in dry film photoresist](#)

Andrés Vásquez Quintero, Danick Briand and Nico F de Rooij

Hybrid additive manufacturing of 3D electronic systems

J Li^{1,5,6}, T Wasley^{1,5}, T T Nguyen¹, V D Ta², J D Shephard², J Stringer³, P Smith³, E Esenturk⁴, C Connaughton⁴ and R Kay¹

¹ Wolfson School of Mechanical and Manufacturing Engineering, Loughborough University, Loughborough, Leicestershire LE11 3TU, UK

² Institute for Photonic & Quantum Sciences, Heriot-Watt University, Edinburgh EH14 4AS, UK

³ Department of Mechanical Engineering, University of Sheffield, Sheffield S3 7RH, UK

⁴ Warwick Mathematics Institute, University of Warwick, Coventry CV4 7AL, UK

E-mail: J.Li5@lboro.ac.uk

Received 28 April 2016, revised 14 June 2016

Accepted for publication 28 June 2016

Published 23 August 2016



Abstract

A novel hybrid additive manufacturing (AM) technology combining digital light projection (DLP) stereolithography (SL) with 3D micro-dispensing alongside conventional surface mount packaging is presented in this work. This technology overcomes the inherent limitations of individual AM processes and integrates seamlessly with conventional packaging processes to enable the deposition of multiple materials. This facilitates the creation of bespoke end-use products with complex 3D geometry and multi-layer embedded electronic systems. Through a combination of four-point probe measurement and non-contact focus variation microscopy, it was identified that there was no obvious adverse effect of DLP SL embedding process on the electrical conductivity of printed conductors. The resistivity maintained to be less than $4 \times 10^{-4} \Omega \cdot \text{cm}$ before and after DLP SL embedding when cured at 100 °C for 1 h. The mechanical strength of SL specimens with thick polymerized layers was also identified through tensile testing. It was found that the polymerization thickness should be minimised (less than 2 mm) to maximise the bonding strength. As a demonstrator a polymer pyramid with embedded triple-layer 555 LED blinking circuitry was successfully fabricated to prove the technical viability.

Keywords: 3D printing, hybrid additive manufacturing, 3D electronic systems, digital light projection stereolithography (DLP SL), 3D micro-dispensing

(Some figures may appear in colour only in the online journal)

1. Introduction

Traditional electronics systems are usually fabricated via printed circuit boards (PCBs), which provide both the electrical interconnections between electronic components and the physical structures for mounting the components [1]. Nowadays, many applications, in particular automotive, industrial systems, medical devices, consumer goods and aerospace, require high value, on-demand, fully functional electromechanical products with complex 3D structures,

which creates challenges in the production of traditional PCB based electronics. Due to the manufacturing flexibility, hybrid additive manufacturing (AM) technology has been hailed to be a potential solution for this purpose [2].

To date, most individual AM processes are generally restricted to one material class and as a result unable to deposit different functional materials within one layer. In order to produce complex, multi-material three-dimensional (3D) structures with embedded electronics, a hybrid AM technology of coupling different digitally driven processes is therefore necessary. This would thereby allow the creation of novel, high-value, bespoke, end-use products with intricate features where the complexity of the geometry or

⁵ These authors contributed equally to this work.

⁶ Author to whom any correspondence should be addressed.

the integration of embedded electronics does not necessarily affect the part's ability to be manufactured cost-effectively.

As early as 1992, research has been undertaken to explore the feasibility of building 3D end-use products with embedded functional components using shape deposition manufacturing (SDM) [3–6]. Kataria *et al* first proposed a method for realising complex devices with embedded functional inserts in stereolithography (SL) [7]. Wicker's group at University of Texas at El Paso introduced a hybrid AM technology integrating dispensing apparatus into a top-down exposure SL system. This technology enabled the integration of direct written circuitries onto the surface of an SL fabricated 3D structures and the creation of a series of 3D electronic systems [8–14]. They further expanded this concept to fused deposition modelling (FDM) and built a 2.5D circuit board for a CubeSat satellite [15]. A Fab@Home system, an open-source AM machine based on a multi-material dispensing process, was developed by Malone *et al* and Periard *et al* for fabricating multi-material electronic devices [16–18]. Sanchez-Romaguera *et al* used multi-material inkjet printing to generate 3D electronic crossovers and interconnections [19].

In order to achieve fine electronic structures ($\sim 10\ \mu\text{m}$ [20]), aerosol jetting was adopted in some hybrid AM technologies. Stratasys and Optomec used aerosol jetting to make circuits, sensors, and antennas onto an unmanned aerial vehicle (UAV) structure which was printed by the FDM process [21]. Similar technology was also tested by Vogeler *et al* for printing interconnections on FDM substrates [22]. Chang *et al* integrated aerosol jetted strain sensor into 3D parts made by PolyJet process [23].

Besides polymer based technologies, other AM technologies have also been explored to realise hybrid AM. Robinson *et al* [24], Siggard *et al* [25] and Li *et al* [26, 27] reported embedding electronics within 3D metal structures made by ultrasonic consolidation. Johander *et al* described the use of ink jet process to make circuitries in 3D printed ceramic parts [28].

As summarised above, most current hybrid AM technologies have been realised by integrating essential AM processes used to fabricate the matrices of the 3D parts with direct writing (DW) process for the printing electronic structures. DW encompasses a number of processes including inkjet printing, dispensing, aerosol jetting, etc, and is capable of printing electronic structures (conductors, insulators, capacitors, antennas, etc) direct from a computer file without any tooling or mask [29]. The features of typical essential AM processes combined with DW processes are stated and compared in table 1.

Based on table 1, it can be concluded that SL process provides high resolution and better compatibility for the integration of electronic structures compared with other AM processes. Thus, SL has been adopted by many researchers in hybrid AM technologies. The majority of SL processes currently used are vector scan-based 'top-down' systems (figure 1). The matrix of the 3D electronic systems were fabricated by selectively laser curing liquid photopolymer in a vat, layer-by-layer, which allows the fabrication of geometrically complex products at a high resolution and fast build time, due to its

working principle of photopolymerization. However, vector scan-based 'top-down' SL process builds the parts from the top downwards and requires a recoating function to planarise the surface before exposure, thus it is not suitable for direct embedding surface mount electronic components which commonly have a height of 1–2 mm [7]. Therefore, premade cavities have to be built for the components, which may adversely affect the integrity of the whole device and are not typically compatible with most conventional pick and place machines. In additional, DW processes are typically restricted to 2D printing of conductive features, and thus the vertical interconnects between parallel circuitry layers had to be created by filling prefabricated cavities with low viscosity conductive material [12]. This method created the potential for bubbles and shorts within the conductors and required an additional thermal curing step. Alternatively most of such interconnects were left on the outer surface of the part [32] causing fractures on the vulnerable conductors and inhibiting the generation of complex multilayer electronic circuits.

This work introduces a hybrid AM technology combining 'bottom-up' digital light projection (DLP) SL process (figure 1(b)) and a 3D micro-dispensing process for the fabrication of 3D electronic systems. This technology allows the direct embedding of dispensed circuitry and the low temperature assembly and packaging of electronic components within a thick polymerized layer. Innovative vertical conductive pillars were created using 3D micro-dispensing process of highly viscous materials to provide reliable interconnections between neighbouring circuitry layers. The effects of the DLP SL embedding on the electrical performance of printed conductor were systematically investigated via four-point probe measurement and non-contact focus variation microscopy. The mechanical strength of SL specimen with the thick polymerized layers was then explored through tensile testing. A pyramid demonstrator embedded with triple-layer 555 LED blinking circuitry was finally fabricated to prove the feasibility of this technology.

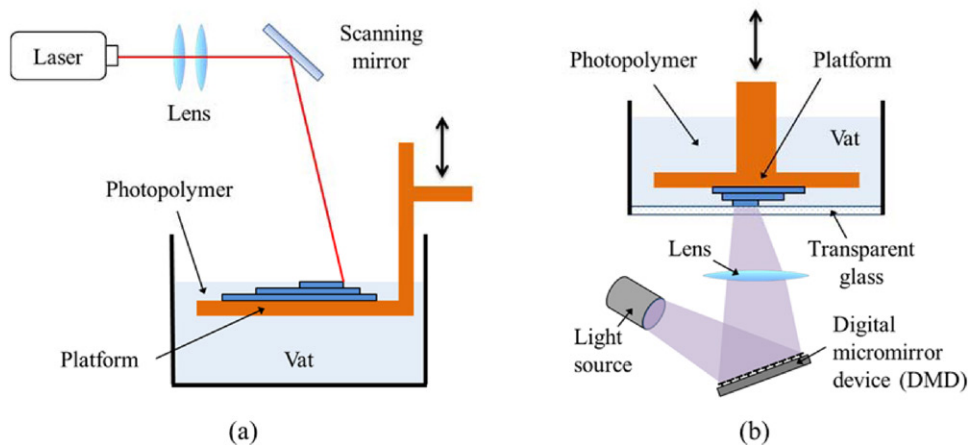
2. Fabrication process

2.1. Process chain

Figure 2 demonstrates the process chain for building 3D electronic systems: firstly, a 'bottom-up' DLP SL 3D printer is used to make the base substrate of the 3D electronic system. An exterior wall is built to provide the external geometry and contain the entire layer of electronics within a build cavity. Both the base substrate and the exterior wall are fabricated through the standard DLP SL fabrication process, and thus the complex geometric details of the package could be maintained. The resin substrate is then cleaned in an ultrasonic bath containing isopropanol to remove any uncured resin residue. After this step the part is aligned and silver electrically conductive adhesive (ECA) is printed on the SL substrate to realise electrical circuitry by a dispensing robot. 3D printed conductive pillars are simultaneously deposited with the circuitry to generate vertical electrical connection between adjacent layers of circuitry. The component interconnects are

Table 1. Advantages and disadvantages of typical essential AM processes used in hybrid AM technologies.

Essential AM process	DW process combined	Examples of hybrid AM technologies	Advantages	Disadvantages
Fused deposition modelling (FDM)	Dispensing and aerosol jetting	[15, 21, 22]	Wide range of FDM materials, low cost of FDM process	Resolution limited by the FDM nozzle orifice diameter ($\sim 254 \mu\text{m}$), difficult to embed parts due to low deposition height
Stereolithography (SL)	Dispensing	[8–14]	High resolution of SL (up to $2 \mu\text{m}$ in X and Y axis [30]), low processing temperature	Limited material selection and high material cost of SL
Material jetting (Polyjet)	Aerosol jetting	[23]	High resolution ($\sim 40 \mu\text{m}$ in X and Y axis for Polyjet), low processing temperature	Limited material selection and high material cost of Polyjet, difficult to embed parts due to low jetting height
Selective laser sintering (SLS)	Aerosol jetting and dispensing	[31]	No need for support structure, multiple objects fabrication in one build process due to ‘nesting’ effect of powder bed	Low resolution, limited SLS materials, high processing temperature of powder sintering (not easily compatible with embedded electronics)
Ultrasonic consolidation (UC)	Dispensing	[24]	Metal part fabrication, hybrid with CNC machining, low processing temperature	Low resolution, high material wastage due to hybrid with a subtraction approach

**Figure 1.** Working principle of the laser-based ‘top–down’ SL process (a) and ‘bottom–up’ DLP SL process (b).

also printed at this stage. Next, surface mount device (SMD) components are placed onto the interconnects and the whole structure is placed into an oven at low temperature to thermally cure the ECA without damaging the photopolymer substrate. The DLP SL process is then employed to embed the whole circuit including silver conductors, electronic components, and the pillars within the same resin layer. Repeating step (b)–(e), a 3D printed structure with an embedded multiple-layer electronic system can be built. Finally, the whole structure is UV post processed to complete the crosslinking of the SL resin.

2.2. DLP SLA process

DLP SL was employed for the polymer matrix fabrication and electronics embedding in this work (figure 1(b)). This technique uses a digital micromirror device (DMD) as a high-resolution dynamic mask for imaging layers in SL

applications [33–35]. This method differs from vector scan-based SL previously used in the fabrication of 3D electronic systems as the photopolymerization is achieved by selectively exposing a complete layer of photosensitive resin to a static projected image for a predetermined period of time rather than tracing out the pattern in a sequential manner using a laser. Thus, with suitable source intensity DLP SL can provide faster build speeds. In addition, the projector can easily be moved up or down to adjust the resolution of the projected image while laser SL normally has a set number of laser spot sizes. With a high resolution DMD in combination with a bespoke lens array, DLP printers can produce a X – Y resolution of $2 \mu\text{m}$ [30]. This therefore makes DLP 3D printing highly accurate and versatile. Moreover, unlike laser SL, DLP does not need multiple moving parts such as X , Y axis stepper motors or a galvanometer for laser beam scanning. This makes DLP SL cheaper and results in greater reliability and easier maintenance.

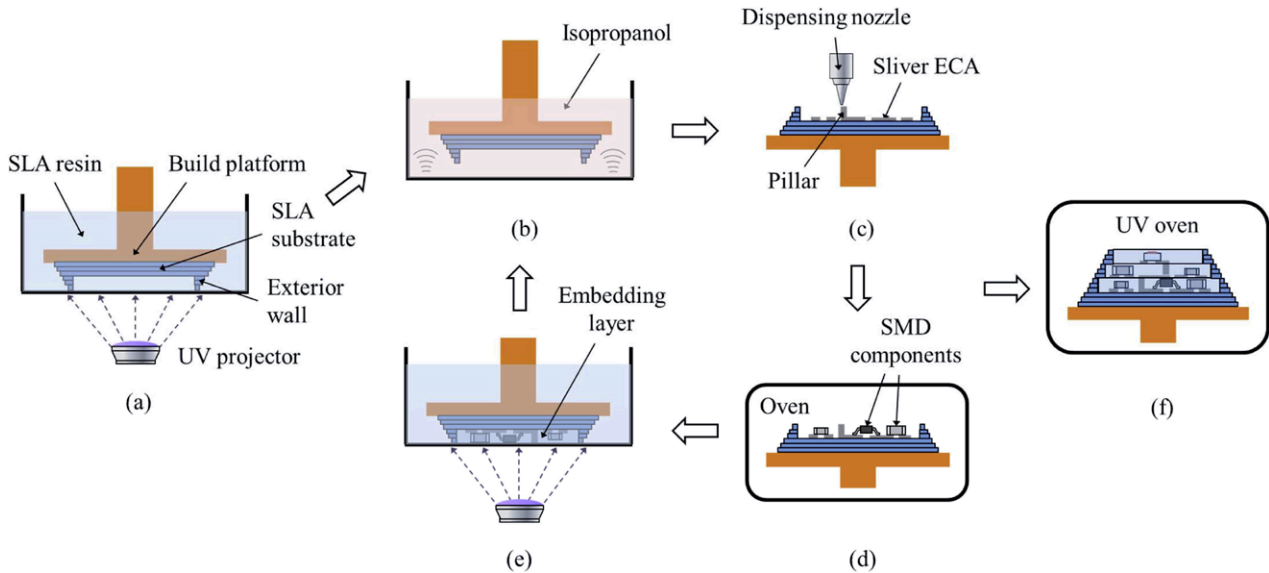


Figure 2. Process chain of the hybrid AM technology for fabricating 3D electronic system. (a) Substrate fabrication. (b) Ultrasonic cleaning. (c) Circuitry dispensing. (d) Components installation and ECA curing. (e) SLA embedding. (f) UV treatment.

An ultraviolet (UV) projection system was positioned underneath a vat with a transparent base, with the projection lens focused onto the centre of the vat. The thickness of the photopolymer layer between the build platform and the vat can then be set and exposed. As the ‘bottom-up’ build orientation was used in this work parts are created upside down. This method enables the direct embedding of printed circuitry together with electronic components in a same polymerized layer (figure 2(e)). Moreover, the resin substrate produced in this way exhibited smoother surface finish as it was polymerized in contact with the base of the vat [36], which was desirable for the dispensing of ECAs. In addition a shallow vat with a very small volume of resin is required, providing the depth of the resin exceeds the predetermined layer thickness.

The DLP SL system used in this work was a modified mUVE 1.5 DLP printer from mUVE 3D. The original white light projector was replaced by a DLP Lightcrafter™ 4500 projection module from Texas Instruments. This projector provides a 405 nm UV LED light source which covers the sensitive wavelength of a variety of commercial photopolymers. The machine was configured to have a 89 mm × 140 mm working area resulting in a minimum resolution of ~100 μm. A further reduction in projection area would require a different set of optics for the projection lens to give a smaller focal area. With altered optics or a higher resolution DLP projector (e.g. DLP Lightcrafter™ 9000 from Texas Instruments) the resolution could be further reduced, however, for proving technical feasibility the current resolution is functional.

A variety of candidate resins were tested in the preliminary experiments. A clear acrylic based resin sensitive to 405 nm wavelength light was found to be the best fit for this work due to two reasons: firstly, the residual stress in the fabricated structure was low after UV exposure and thermal treatment, thus there was no obvious deformation in the finished sample; secondly, its glass transition temperature (T_g) after polymerization was up to 100 °C, much higher than other candidates’.

Consequently, a higher temperature could be used in the thermal curing of printed ECAs to achieve superior electrical conductivity.

2.3. Cleaning module

After the substrate fabrication (figure 2(a)) or the circuitry embedding (figure 2(e)), an ultrasonic agitation cleaning stage was conducted to remove any uncured resin from the parts before the parts were dried using a high pressure source of clean dry air, to dry the surface. Isopropanol was selected as the rinse medium due to no obvious degradation or damage being found on the resin substrate after cleaning.

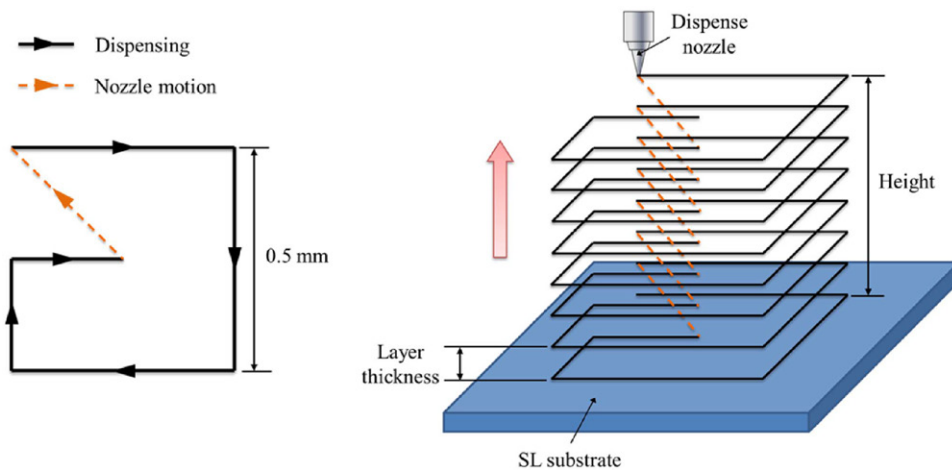
2.4. Dispensing process

The dispensing process is one of a variety of DW technologies by which a wide range of functional and/or structural paste materials (polymer, ceramic, and metallic) can be precisely deposited onto a substrate in a digitally defined way [37]. By combining a laser positioning feedback system and alignment camera, the dispensing process allowed precise conformal deposition on uneven substrates, therefore ideal for printing multilayer circuitry.

2.4.1. Dispensing equipment. A Musashi Shotmaster 500 dispensing system was used to dispense the circuitry. This system is comprised of five main parts: a 3-axis CNC router, a computer controller, a digitally controlled dispenser (a syringe connected with a pneumatic driven pump), an alignment camera, and a laser positioning feedback system. To enable dispensing, the pattern of circuitry was first designed with MuCAD® IV software relative to a predefined origin and the ECA was loaded into a syringe. Then, the camera was used to identify fiducial marks on the substrate for alignment. Subsequently, a laser was used to scan the top surface following the

Table 2. Product properties of two silver filled ECAs.

	EPO-TEK® EJ2189	EPO-TEK® E4110-PFC
Type	2-part	2-part
Mix ratio by weight	10:1	3:1
Pot life	4 h	2–3 h
Viscosity	Viscosity (@ 1 RPM/23 °C): 55 000–90 000 cPs	Viscosity (@ 5 RPM/23 °C): 50 000–60 000 cPs
Particle size	≤45 μm	≤20 μm
Volume resistivity at 23 °C	≤5 mΩ cm	≤5 mΩ cm
Cure condition	15 mins at 150 °C 1 h at 100 °C 3 h at 80 °C 3 d at 23 °C	1 h at 120 °C 3 h at 80 °C 6 h at 45 °C

**Figure 3.** Schematic diagram of conductive pillar printing.

designed nozzle path to obtain the surface morphology. This morphology data allows automated adjustment of the nozzle height to maintain a constant print gap by accommodating any unevenness in substrate surface. Finally the pattern of circuitry was automatically dispensed onto the substrate. The pneumatic pressure for ECA extrusion was produced by the Musashi Super Σ ®CMII digital control dispenser. It provides a wide range of pressure from 30.0 kPa to 500.0 kPa facilitating the printing of the high viscosity, heavily loaded silver ECAs to produce conductive traces and interconnects (up to 1000 Pa s [38]). The CNC router is digitally driven enabling high positioning accuracy ($\pm 5 \mu\text{m}$) and fast printing speed (0.1 mm s^{-1} – 300 mm s^{-1}).

The quality of printed circuitry was highly dependent on five parameters: (1) viscosity of the dispensed material, (2) inner diameter (ID) of the dispensing nozzle, (3) extrusion pressure, (4) print speed of the nozzle, and (5) dispensing gap (distance from the tip of nozzle to the substrate). For the ECAs used in this work, the pot life was more than 3 h so the viscosity could be regarded as constant during the dispensing process. To avoid any potential clogging a stainless steel high-precision nozzle with the ID of $250 \mu\text{m}$ was selected since the orifice is at least 5 times larger than the maximum particle size of the ECA ($\sim 45 \mu\text{m}$). When the viscosity and nozzle ID were determined, the pressure, print speed and dispensing height were systematically investigated to achieve the optimal features for the designed circuitry as covered in section 3.2.

2.4.2. Dispensing materials. Two silver filled ECAs were selected as the conductive materials for the printed circuitry since they could be thermally cured at temperatures below $100 \text{ }^\circ\text{C}$ (table 2) [39, 40]. This made them compatible with the SL resin matrix which itself, possesses a low glass transition temperature. Both ECAs were designed for electronic assembly so SMD components could be directly adhered onto printed connecting pads making additional bonding materials unnecessary.

2.4.3. Vertical pillar printing. Vertical pillars were firstly developed in this work for realizing reliable interconnects between circuitry layers. Due to the high resolution of the dispensing equipment and high viscosity of the ECAs, free-standing pillars could be printed layer-by-layer (figure 3). The maximum potential height of the pillar was determined by the material properties of the ECAs (particularly viscosity), pillar size and dispensing toolpath. In this work, the nozzle path used was a clock-wise square helix with 0.5 mm width.

3. Experimental characterization

Three issues must be systematically investigated to prove the feasibility of the hybrid AM technology mentioned above: (1) the practicality of polymerizing a thick layer with ‘bottom up’ DLP SL process and the resultant effects on mechanical

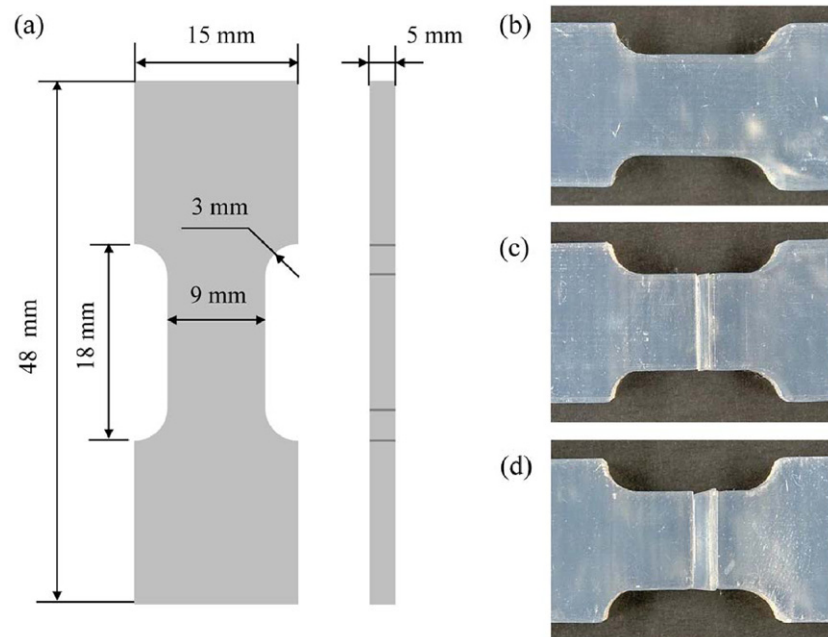


Figure 4. Tensile testing specimens: (a) design, (b) type 1 with standard $100\ \mu\text{m}$ layer thickness, (c) type 2 with 1 mm exposure layer, and (d) type 3 with 2 mm exposure layer.

strength of the fabricated components; (2) the topology of dispensed conductive traces and pillars; and (3) the effects of curing conduction and SL embedding on the conductivity of the silver conductive materials.

3.1. Characterisation of thick-layer polymerization

A typical exposure thickness for the SL process is around $100\ \mu\text{m}$ or less. However, due to the greater thickness of SMD components thick-layer polymerization was required in order to embed the packaged components and circuitry. To investigate the practicality of this solution and its potential effects on the mechanical strength three types of ‘dog bone’ shape specimens were fabricated on the DLP SL system, based on the design shown in figure 4. Type 1 was built via regular $100\ \mu\text{m}$ thick exposures without interruption (figure 4(b)), while type 2 was interrupted halfway through fabrication and ultrasonically cleaned. A single 1 mm layer was then polymerized on the half-finished specimen before the rest of the part was completed using the standard $100\ \mu\text{m}$ exposure thickness (figure 4(c)). Type 3 was also prepared as the same manner as type 2 but the thickness of middle layer was changed to 2 mm (figure 4(d)). 1 mm and 2 mm thick layers could be successfully polymerized using 90s and 210s exposures of the UV DLP projection system.

For each type of specimen, six samples were fabricated and tensile tested using an Instron 3369 tensile testing machine. The fracture modes of tested samples are shown in figure 5. For type 1, four specimens fractured across the layer interface and the other two on the layer interfaces. Similar results were also found in type 2 where the ratio between the specimens that cracked on and across layer interface was 1:1. This indicated that for type 1 and 2 samples the adhesive strength between SL layers was equivalent to the tensile strength of the

polymerized resin. However, only the interface failure mode was observed in type 3 samples, revealing the degradation of mechanical strength on the curing interface when a thicker embedding layer was used.

The maximum tensile loads of all three types of specimens are plotted in figure 6. The average maximum tensile load of type 1 specimens was 1565 N. This can be used as the reference to evaluate the influence of thick-layer polymerization on mechanical strength. Type 2 specimens exhibited similar results as type 1 with only a small reduction in load at failure of 25 N. For type 3 samples, the tensile load reduced to 1241 N, a decrease of about 20% compared with that of type 1 and 2. These results confirmed the findings from the fracture mode investigation. According to the fracture modes and peel loads, the polymerization thickness should be minimised, as the bonding strength reduces as layer thickness increases.

3.2. Topology of conductive traces and pillars

Accurate control of the line width of the conductor is key for achieving high integrity of the electronic systems. Moreover, the geometry determines the resistance of printed conductors regardless of the electrical resistivity of the conductor material. For the pillars, due to the rheology of ECAs, slumping might happen during the layer-by-layer dispensing. Thus, the final 3D profiles of the conductors and pillars need to be analysed. Through accurate topology measurement, the effects of curing conditions on the morphology of dispensed conductors can be explored. Three different curing regimes were selected in accordance with product datasheets: 1 h at $100\ ^\circ\text{C}$, 3 h at $80\ ^\circ\text{C}$, and 6 h at $45\ ^\circ\text{C}$. Each curing regime was applied to test samples before an Alicona InfiniteFocus® G4f non-contact focus variation microscopy system was employed to obtain profile data of the conductive traces and pillars.

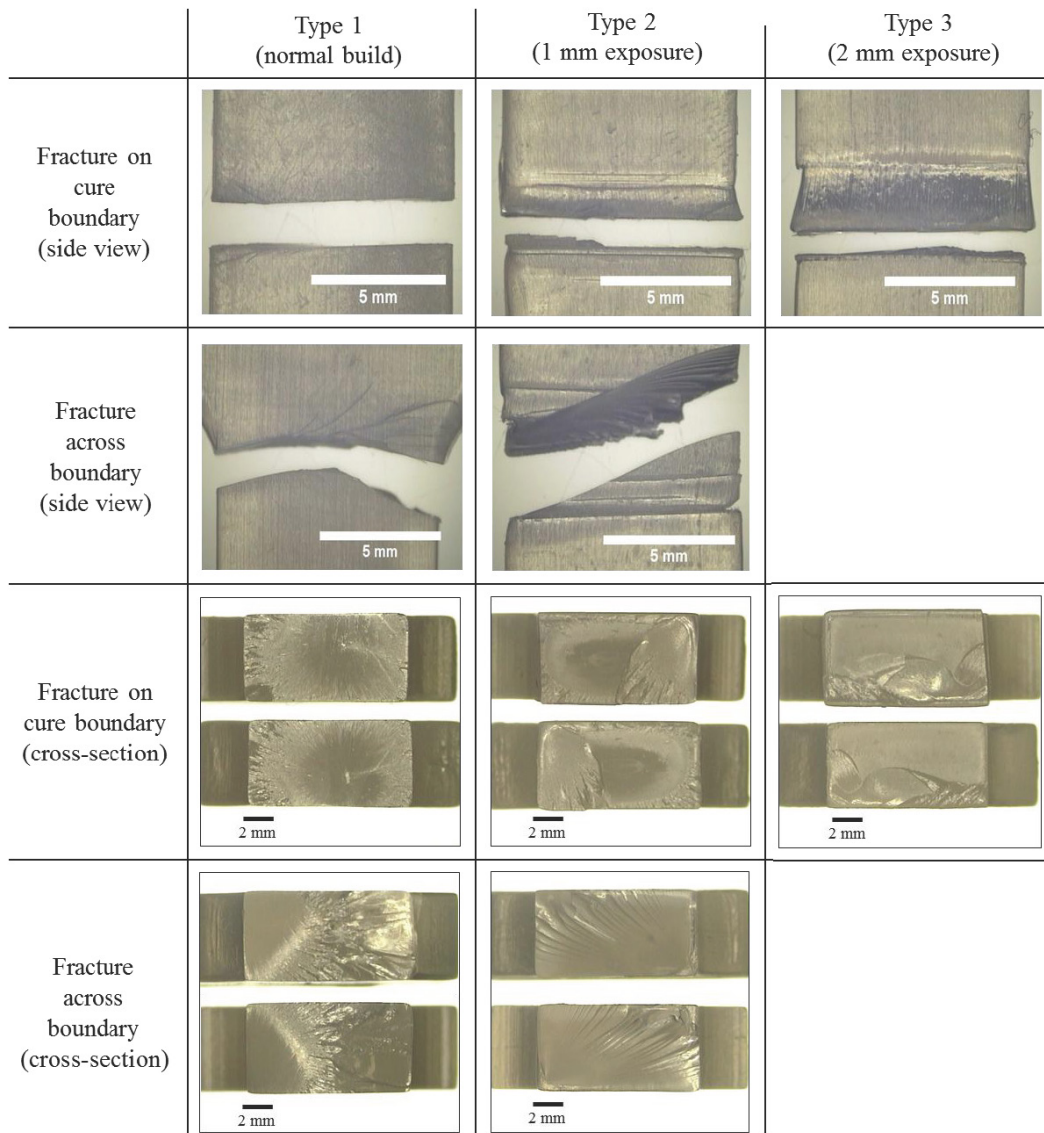


Figure 5. Fracture modes of the specimens during tensile testing.

The dispensing nozzle used in this work was a stainless high precision nozzle with the ID of 250 μm with the print gap kept at a value equal to the ID. Through systematic testing, the optimal extrusion pressure acquired was 60 kPa for material EJ2189 and 340 kPa for material E4110-PFC, where the print speed was 4 mm s⁻¹ for both materials. Although the viscosity ranges of both ECAs are similar according to the technic data sheets from manufacturer (table 2), the latter appeared to be more viscous in practical dispensing, requiring a dispensing pressure approximately 6 times higher than the former.

A 10 \times objective lens was used to obtain the profiles of conductive traces. For each curing condition and each type of silver ECA, five traces were prepared for each set of parameters mentioned previously and three scanning areas were taken randomly along the central line of each trace to obtain the average line width and height. Similarly, for the pillars, five structures were printed for each combination of parameters, and a 5 \times object lens was used to scan their profiles. The peak height and base diameter of each pillar could then be extracted from the profile data.

For both ECAs, no obvious differences before and after curing were found in the profile data. The representative profiles of EJ2189 and E4110-PFC were shown in figure 7. E4110-PFC exhibited a more regular semicircular profile with smooth surface finish than EJ2189, and its average line width and height were approximately 370 μm and 160 μm respectively, while for EJ2189 these values were approximately 410 μm and 165 μm . This could be attributed to the higher viscosity of E4110-PFC, limiting the slumping of the silver paste and better maintaining the original shape of the printed traces.

Similar results were also observed in pillar printing at the same 4 mm s⁻¹ print speed (figure 8). The higher viscosity E4110 allowed better support and shape maintenance, and thus 16 dispensed layers could be printed concurrently, one on top of the other. Any further increase in number of dispensed layers started to cause distortion or collapsing of the pillar. For the design of 0.5 mm side width square helix, the maximum height achieved was 3.8 mm with a base width of 0.9 mm creating a feature with an aspect ratio of about 4.2. In comparison, EJ2189 could only produce a 1.8 mm high,

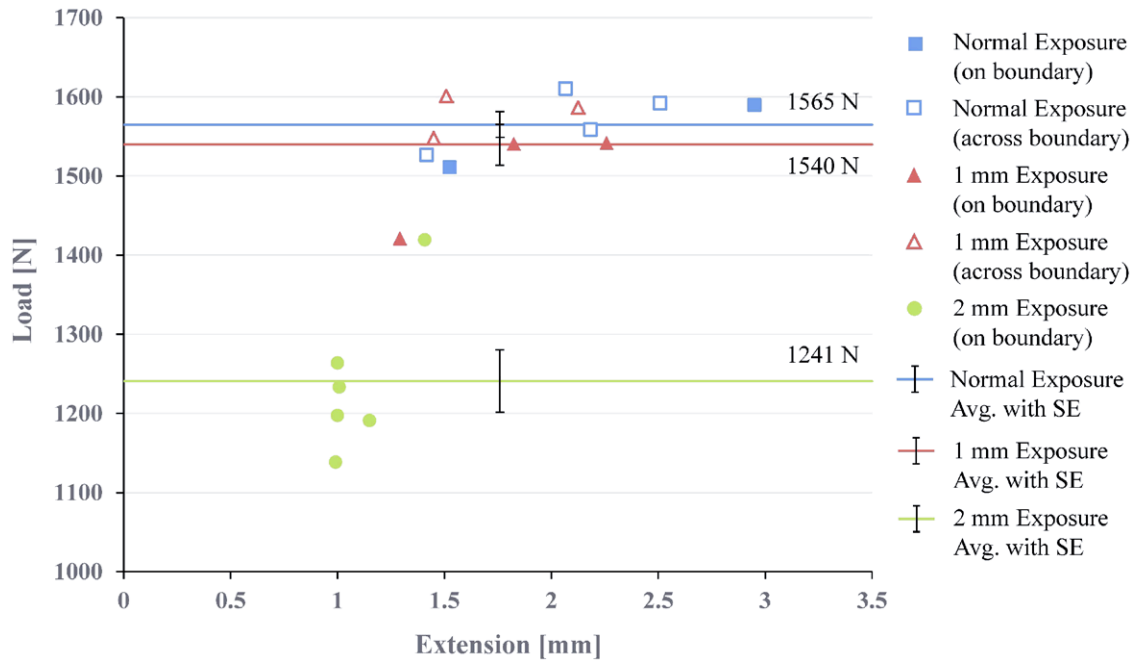


Figure 6. Tensile failure loads of three types of specimens.

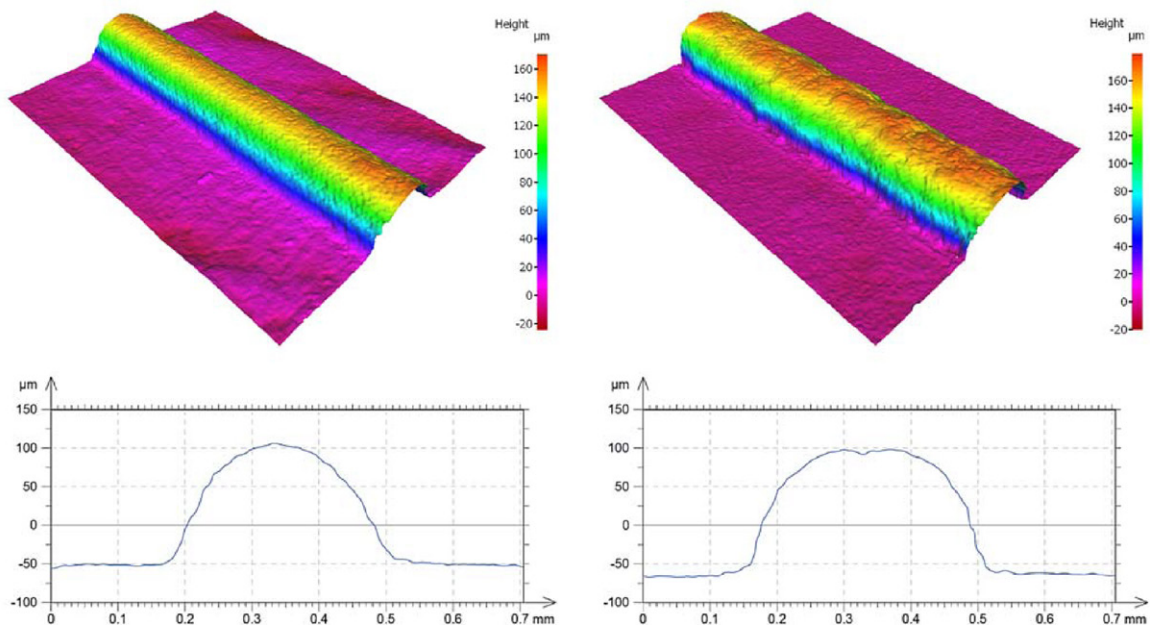


Figure 7. Profile data of conductive tracks printed in (a) E4110-PFC and (b) EJ2189 Conductive epoxies and thermally cured at 80 °C for 3 h.

1 mm wide pillar with an aspect ratio of 1.8 via 10 layers of dispensing.

Based on the profile results of conductive traces and pillars, it was found that the viscosity played a vital role in circuitry dispensing, especially when trying to precisely control the size of these structures. Higher viscosity conductive materials limited the shape deformation due to the slump, and aided in the realisation of thinner traces and higher aspect ratio pillars. These properties enable the elimination of short connections in the circuit, and more importantly, the miniaturization of the size of the whole electronic system, considered a major advantage in the electronic industry in

order to increase functionality and produce smaller, more portable devices.

The cross-sections of the pillars printed in E4110-PFC and EJ2189 are shown in figure 9. Voids were observed in the pillars made of both conductive epoxies. They were probably caused by the air that was encapsulated either in the epoxy preparation (mixing resin with hardener manually) or during the square-helix pillar printing. For EJ2189, due to its lower viscosity the encapsulated air bubbles could escape much more easily. Therefore, compared with E4110-PFC pillars, the voids in EJ2189 pillars are much smaller and less abundant. To achieve solid pillars, some degassing techniques

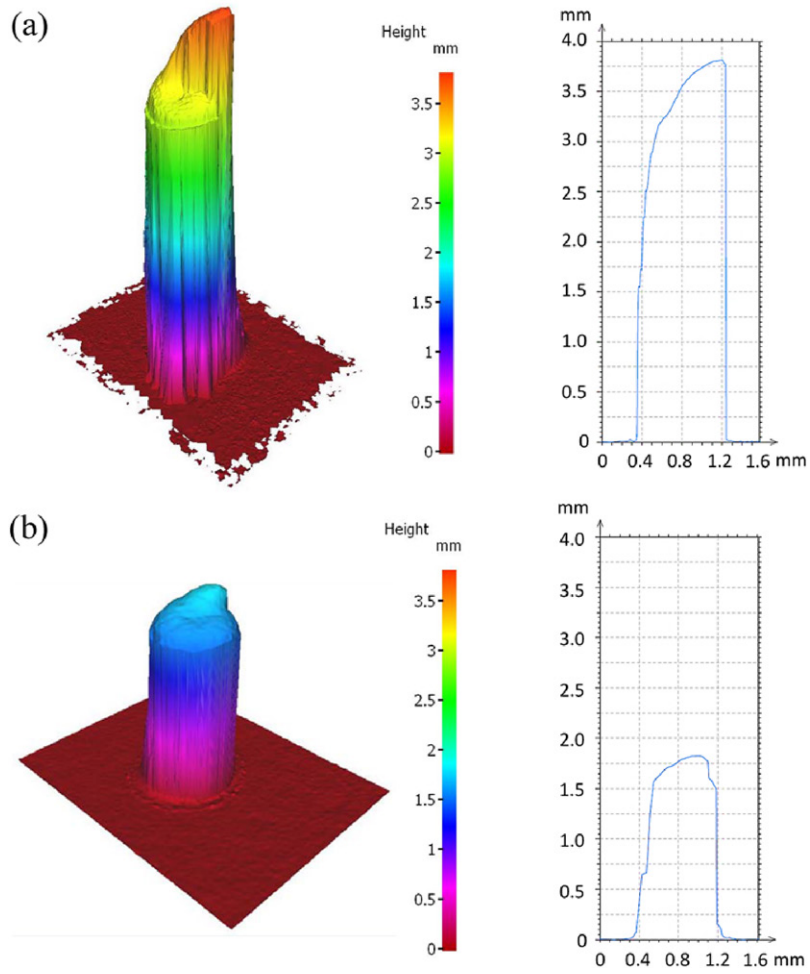


Figure 8. Profile data of pillars printed in (a) E4110-PFC and (b) EJ2189 conductive epoxies and cured at 80 °C for 3h.

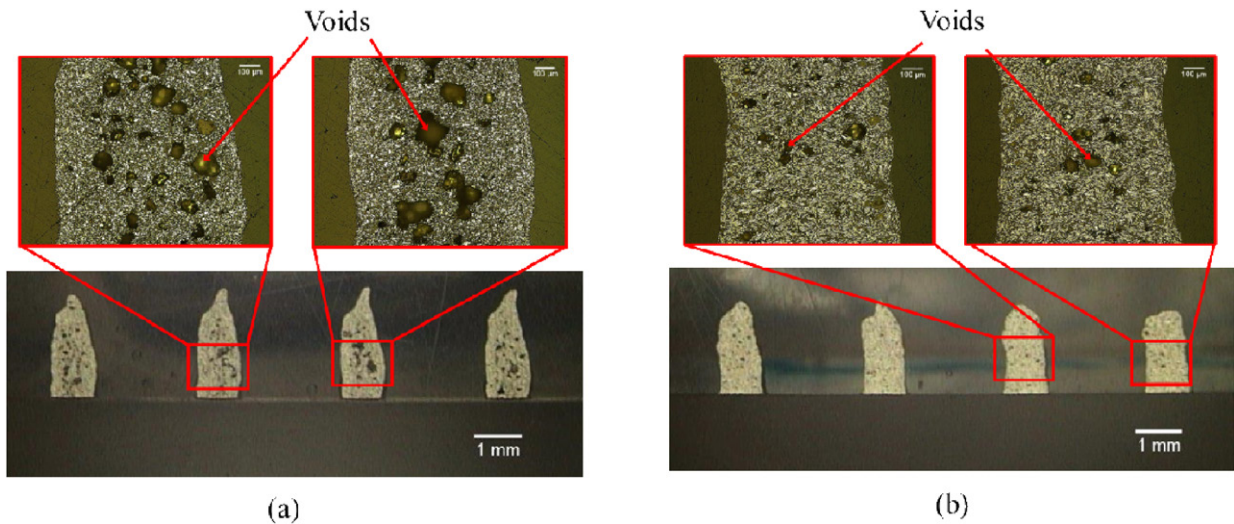


Figure 9. Cross-section of pillars printed in (a) E4110-PFC and (b) EJ2189 conductive epoxies and cured at 80 °C for 3h.

such as vacuum degassing could be applied in the fabrication process.

3.3. Resistivity of conductive traces

To identify the effects of curing conditions and DLP SL embedding on the functionality of printed conductors, the resistivity

of the printed conductors cured under three different conditions was investigated, both before and after SL embedding.

Four-point probe measurements were taken to measure the electrical resistance of the printed conductors using a Keithley 580 $\mu\Omega$ m (Keithley Instruments Inc., Ohio, USA). According to Ohm's law, the resistance of the whole conductor, R (Ω), was calculated using the following equation:

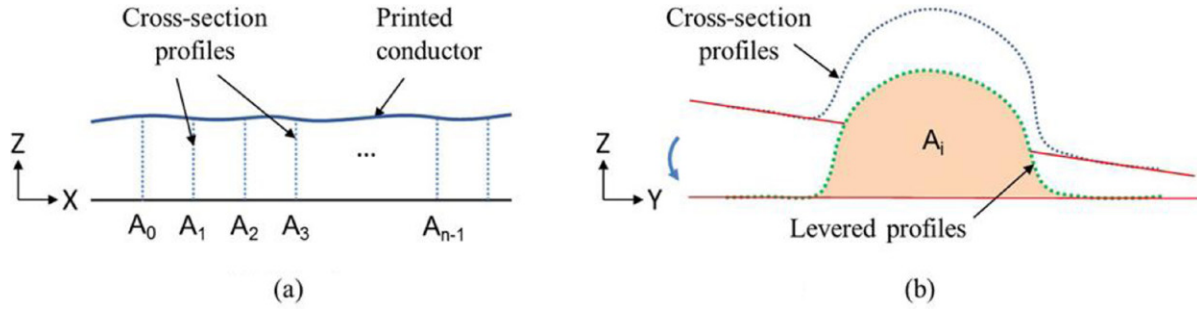


Figure 10. Schematic diagram of RANSAC method for obtaining the cross-sectional areas of the scanned conductor. (a) Side view. (b) Cross-section view.

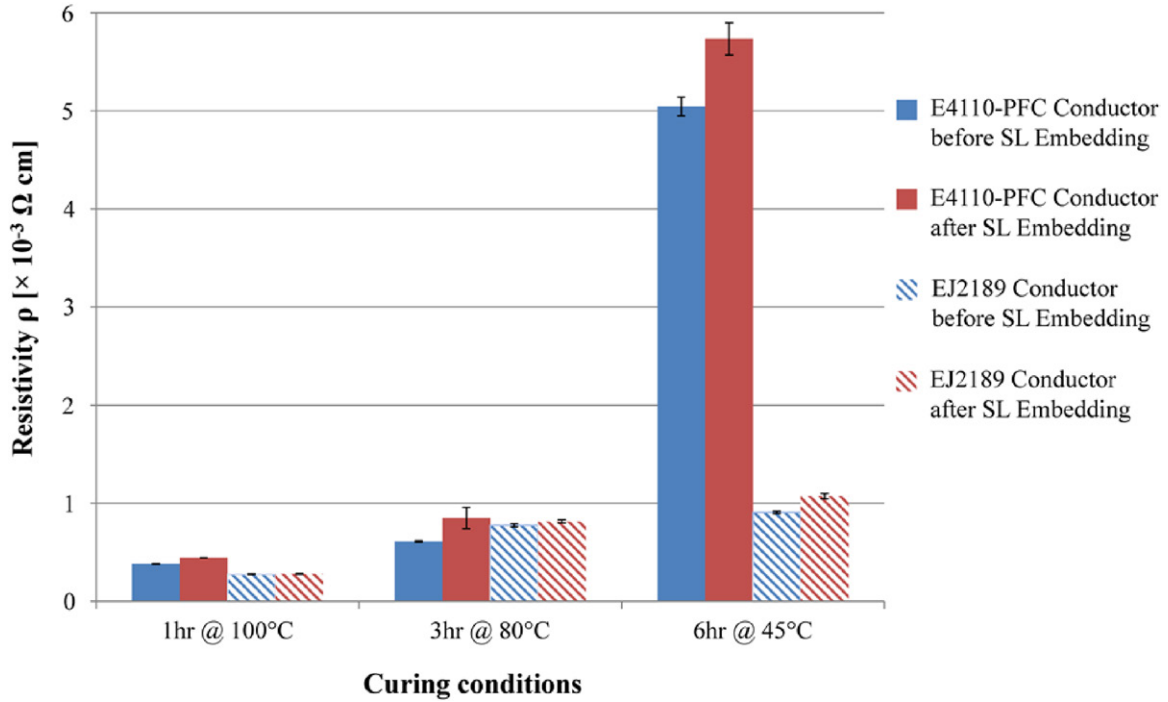


Figure 11. The average resistivity of E411-PFC and EJ2189 ECAs before and after DLP SL embedding under three different curing conditions.

$$R = \rho \frac{L}{A} \quad (1)$$

where ρ (Ω cm) is the resistivity, L (cm) is the length of the conductor and A (cm^2) is cross-section area of the conductor. The resistance of the individually scanned sections R' (Ω) can therefore be described using the following equation in which they are expressed as a ratio of the sections length L' (cm) to the total length of the conductor L (cm) (2 cm in this case) multiplied by the total resistance, R (Ω).

$$R' = \frac{L'}{L} R. \quad (2)$$

The Alicona scanning file consisted of a matrix of data points with 3D coordinate values, and thus a series of cross-sectional profiles of the conductor could be extracted from the file (figure 10). A MATLAB[®] programme based on the random sample consensus (RANSAC) [41] was generated to extract cross-section profiles and calculate the average cross-sectional areas of the scanned sections (figure 10(a)). During the processing, the RANSAC programme was applied to the

substrate portions of the scanned profile (figure 10(b)) and fitted with a straight line through the cross-section. The fitting line, together with the dataset, was horizontally levelled to a reference plane in order to compensate for any slope of the substrate during Alicona measurement (figure 10(b)). The cross-sectional area of the conductive trace was then determined by the region between the conductor portion of the profile and the horizontal axis.

Therefore, the average cross-section area A_a (cm^2) could be calculated via the MATLAB[®] programme as:

$$A_a = \frac{1}{n} \sum_{i=0}^{n-1} A_i \quad (3)$$

where A_i (cm^2) is the cross-section area of each profile and n is the quantity of profiles in one scanned section. With equations (1)–(3), the resistivity of printed conductor could be calculated as:

$$\rho = R \frac{A_a}{L}. \quad (4)$$

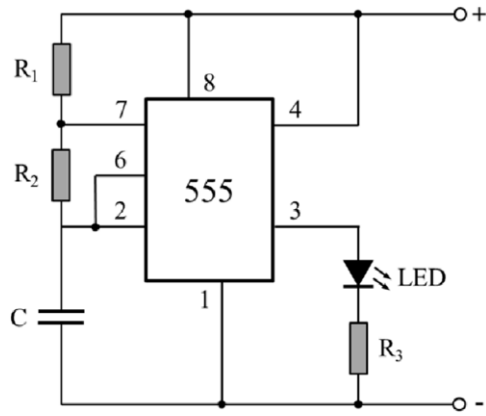


Figure 12. Circuit diagram of the 555 timer based blinking LED circuit.

For each curing condition, five conductors were printed on SL substrates with a 250 μm ID nozzle for both E4110-PFC and EJ2189 ECAs. With the profile data from Alicona scanning, the MATLAB[®] programme based on RANSAC method obtained the average cross-section area of the conductors. Four-point probe measurements were performed before and after SL embedding. 1.5 mm was chosen as the embedding layer thickness, because it was thick enough to fully embed the SMD components used in this work (0603 SMD components and thin-shrink small outline packaged (TSSOP) chips). The average resistivity before and after SL embedding was calculated via equation (4) and then plotted in figure 11. As the curing temperature increased, the resistivity of E4110-PFC conductors reduced significantly from around $5 \times 10^{-3} \Omega \cdot \text{cm}$ (cured at 45 °C) to around $4 \times 10^{-4} \Omega \cdot \text{cm}$ (cured at 100 °C). The same tendency was also observed in EJ2189 conductors that show a resistivity decrease from about $1.0 \times 10^{-3} \Omega \cdot \text{cm}$ (cured at 45 °C) to about $2.8 \times 10^{-4} \Omega \cdot \text{cm}$ (cured at 100 °C). With increased curing temperature, the curing time for both ECAs was also significantly shortened from 6 h to 1 h. When the curing temperature was higher than 80 °C, there was nearly no obvious difference of the resistivity for both ECAs before and after SL embedding. Thus, it could be concluded that when the curing condition is sufficient the ECAs used in this work are compatible with the DLP SL embedding process. 80 °C for 3 h produced nearly identical resistivity for both ECAs, whereas at 100 °C for 1 h EJ2189 showed a lower resistivity of $\sim 4 \times 10^{-4} \Omega \cdot \text{cm}$ compared with $\sim 2.8 \times 10^{-4} \Omega \cdot \text{cm}$ of E4110-PFC. This is probably due to the larger silver particles loaded in EJ2189 (table 1). These have a larger surface area, and could therefore form more surface contact and as a result, more conductive pathways in the conductors, reducing resistance [42].

4. Demonstrators

4.1. Working principle

A polymer pyramid embedded with a triple-layer 555 timer based blinking LED circuit was fabricated as a demonstrator. The circuitry includes an 8-pin TSSOP 555 timer and five

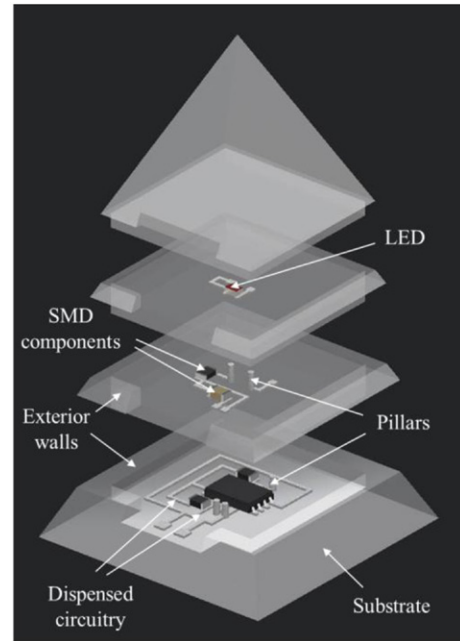


Figure 13. Exploded schematic showing the pyramid demonstrator.

Table 3. The dimensions of the SMD components used in the demonstrator.

	TSSOP 555 timer	LED	0603 SMT capacitor	0603 SMT resistor
Length (mm)	6.4	1.6	1.6	1.6
Width (mm)	3	0.8	0.8	0.8
Height (mm)	1.2	0.8	0.8	0.45

SMD electronic components (three resistors, one capacitor, one LED) as shown in figure 12.

Theoretically, the frequency of the astable circuit is dependent upon the value of R_1 , R_2 , and C , and can be calculated as the equation below:

$$f = \frac{1}{0.693C(R_1 + 2R_2)} \quad (5)$$

where f (Hz) is the frequency of the blinking circuit. In this case, the value of R_1 , R_2 , and C are 100 k Ω , 22 k Ω , and 10 μF , respectively, and as a result the frequency of the circuit according to equation (5) is 1 Hz. R_3 is a 1 k Ω resistor used to limit the current through the LED.

4.2. Design and fabrication

The design and the fabrication steps are shown in figure 13. The pyramid demonstrator has base dimensions and height of 20 mm \times 20 mm and 20 mm, respectively. The 555 timer circuit is separated into three layers connected via vertical pillars. The substrate was made by the SL process, and an exterior wall provides the external geometry and contains the embedded layer of electronics that was also built in this step. The exterior wall was fabricated through standard DLP SL fabrication process with the polymerization layer thickness of 100 μm , so the complex details of external geometry could

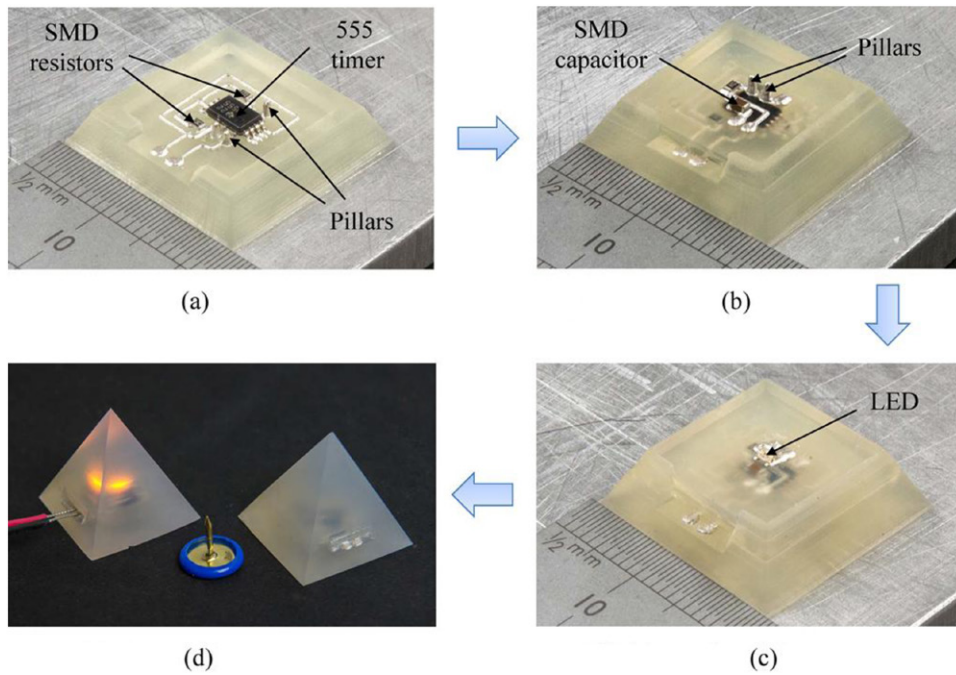


Figure 14. The fabrication steps of the pyramid demonstrator. (a) First layer circuitry. (b) Second layer circuitry. (c) Third layer circuitry. (d) Finished samples.

be maintained. Then, the first layer of circuitry including three vertical pillars was dispensed, and R_1 , R_2 and TSSOP 555 timer chip were mounted on the printed pads. The overall dimension of the printed circuitry was only $10\text{ mm} \times 10\text{ mm}$. The whole structure was cured in a thermal oven (WN60, Lenton Furnaces & Ovens). Subsequently, the first layer of circuitry was embedded and the exterior wall of the second layer was simultaneously fabricated. After repeating this process chain a third time and adding the apex geometry, the pyramid structure embedded with three-layer circuitry was successfully completed.

The dimensions of the electronic components used in this work are stated in table 3. The thickest component used in this demonstrator is a TSSOP 555 timer chip with a height of 1.2 mm. Accordingly, a thickness of circuitry embedding layer was set to 1.5 mm to fully encapsulate all the components. The polymerization time for such layer was 120 s, obtained via systematic testing. EJ2189 was chosen as the conductive material for circuitry dispensing due to its higher electrical conductivity compared with E4110. Although the lower viscosity of EJ2189 caused some slump of the printed structures, it was still viscous enough to produce a clear circuit layout for the demonstrators and the vertical pillars with a height of around 1.5 mm. The nozzle used in dispensing was a $250\ \mu\text{m}$ ID stainless steel nozzle, and the print parameters were $250\ \mu\text{m}$ print gap, 60 kPa extrusion pressure and 4 mm s^{-1} print speed.

4.3. Finished samples

The finished demonstrator shown in figure 14(d) and the details of all three layers of electronics are illustrated in figures 14(a)–(c). When a 9 V power source was applied, the

LED blinked with a frequency of $\sim 1.1\text{ Hz}$, close to the calculated value.

Compared with currently used hybrid AM technologies, this technology could provide more reliable electrical connections with high conductivity since the vertical pillars and the printed circuitry were fully cured before SL embedding. Moreover, the printed circuitry and pillars were totally embedded within the polymer matrix protecting the vulnerable electrical structure from the external environment.

5. Conclusion

This work presents a novel hybrid AM technology combining DLP SL process and dispensing process alongside conventional surface mount packaging for the fabrication of complex multilayer 3D electronic systems. This method allows the cost-effective production of bespoke sensor systems and electronics for a range of industries such as medical, automotive, aerospace and industrial systems.

A ‘bottom up’ DLP SL system was employed to fabricate a polymer matrix and directly embed the printed circuitry and electronic components within a thick polymer layer. Tensile testing, found that the bonding strength of the thick embedding layer reduced as the layer thickness increased. At a value of 1 mm the tensile strength between polymerised layers was maintained and close to the tensile load of the samples made with standard polymerization layer thickness (0.1 mm), 1565 N.

A dispensing process was used to print electrical conductors and interconnects. Innovative freestanding conductive pillars were created to provide through layer electrical connections in the same stage. After surface mount assembly of electronic components the printed circuitry was thermally

cured and then fully embedded within the polymer matrix. Two low curing temperature ECAs, E4110-PFC and EJ2189, were tested during experimentation. When the curing temperature was higher than 80 °C, both ECAs displayed high electrical conductivity, exceeding the values on their data sheets, and no negative effect of SL embedding on the conductivity was observed.

A pyramid embedded with three-layer 555 LED blinking circuitry was successfully fabricated as a demonstrator proving the feasibility of the hybrid AM technology. For DLP SL process, the X–Y resolution can be improved to 2 μm [30], and 5 μm ID nozzle is now available in market for dispensing process. This technology could therefore be used to fabricate 3D customized micro electronic systems with highly complex internal and external geometries.

Acknowledgments

This work is funded by the UK Engineering and Physical Sciences Research Council under grants EP/L017431/1, EP/L017350/1, EP/L016907/1 and EP/L017415/1.

References

- [1] Khandpur R S 2006 *Printed Circuit Boards Design, Fabrication, Assembly and Testing* (New York: McGraw Hill Professional)
- [2] O'Donnell J, Ahmadvanlou F, Yoon H-S and Washington G 2014 All-printed smart structures: a viable option? *Proc. SPIE* **9057** 905729
- [3] Beck J E, Prinz F B, Siewiorek D P and Weiss L 1992 Manufacturing mechatronics using thermal spray shape deposition *Proc. of the 1992 Solid Freeform Fabrication Symp.* pp 272–9
- [4] Cham J, Pruitt B, Cutkosky M R, Binnard M, Weiss L E and Neplotnik G 1999 Layered manufacturing with embedded components: process planning considerations *Proc. DETC99 1999 ASME Design Engineering Technical Conf.* pp 1–9
- [5] Weiss L E, Prinz F B, Neplotnik G, Padmanabhan P, Schultz L and Merz R 1996 Shape deposition manufacturing of wearable computers *Proc. of the 1996 Solid Freeform Fabrication Symp.* pp 10–2
- [6] Weiss L E, Merz R, Prinz F B, Neplotnik G, Padmanabhan P, Schultz L and Ramaswami K 1997 Shape deposition manufacturing of heterogeneous structures *J. Manuf. Syst.* **16** 239–48
- [7] Kataria A, Rosen D W, Kataria A and Rosen D W 2001 Building around inserts: methods for fabricating complex devices in stereolithography *Rapid Prototyping J.* **7** 253–62
- [8] Castillo S, Muse D, Medina F, Macdonald E and Wicker R 2009 Electronics integration in conformal substrates fabricated with additive layered manufacturing *Proc. of the 20th Annual Solid Freeform Fabrication Symp.* pp 730–7
- [9] De Nava E, Navarrete M, Lopes A, Alawneh M, Contreras M, Muse D, Castillo S, Macdonald E and Wicker R 2008 Three-dimensional off-axis component placement and routing for electronics integration using solid freeform fabrication *Proc. of the 19th Annual Solid Freeform Fabrication Symp.* pp 362–9
- [10] Lopes A J, Navarrete M, Medina F, Palmer J A, Macdonald E and Wicker R B 2006 Expanding rapid prototyping for electronic systems integration of arbitrary form *Proc. of the 2006 Solid Freeform Fabrication Symp.* pp 644–55
- [11] Lopes A J, MacDonald E and Wicker R B 2012 Integrating stereolithography and direct print technologies for 3D structural electronics fabrication *Rapid Prototyping J.* **18** 129–43
- [12] Medina F, Lopes A, Inamdar A, Hennessey R, Palmer J, Chavez B, Davis D, Gallegos P and Wicker R 2005 Hybrid manufacturing: integrating direct-write and stereolithography *Proc. of the 2005 Solid Freeform Fabrication Symp.* pp 39–49
- [13] Navarrete M, Lopes A, Acuna J, Estrada R, Macdonald E, Palmer J and Wicker R 2007 Integrated layered manufacturing of a novel wireless motion sensor system with GPS *Proc. of the 18th Annual Solid Freeform Fabrication Symp.* pp 575–85
- [14] Palmer J A, Davis D W, Gallegos P L, Medina F, Summers J L, Chavez B D and Wicker R B 2005 Realizing 3-D interconnected direct write electronics within smart stereolithography structures *Proc. of the ASME 2005 Int. Mechanical Engineering Congress and Exposition* pp 287–93
- [15] Espalin D, Muse D W, MacDonald E and Wicker R B 2014 3D Printing multifunctionality: structures with electronics *Int. J. Adv. Manuf. Technol.* **72** 963–78
- [16] Periard D, Malone E and Lipson H 2007 Printing embedded circuits *Proc. of the 18th Solid Freeform Fabrication Symp.* pp 502–12
- [17] Malone E and Lipson H 2006 Freeform fabrication of ionomeric polymer-metal composite actuators *Rapid Prototyping J.* **12** 244–53
- [18] Malone E, Berry M and Lipson H 2008 Freeform fabrication and characterization of Zn-air batteries *Rapid Prototyping J.* **14** 128–40
- [19] Sanchez-Romaguera V, Madec M-B and Yeates S G 2008 Inkjet printing of 3D metal–insulator–metal crossovers *React. Funct. Polym.* **68** 1052–8
- [20] Perez K B and Williams C B 2014 Design considerations for hybridizing additive manufacturing and direct write technologies *Proc. of ASME 2014 Int. Design Engineering Technical Conf. & Computers and Information in Engineering Conf.* pp 1–12
- [21] Paulsen J A, Renn M, Christenson K and Plourde R 2012 Printing conformal electronics on 3D structures with aerosol jet technology *Proc. of the 2012 Future of Instrumentation International Workshop (FIIW)* pp 47–50
- [22] Vogeler F, Verheeecke W, Voet A and Valkenaers H 2013 An initial study of aerosol jet[®] printed interconnections on extrusion-based 3d-printed substrates *vog Stroj. Vestn. J. Mech. Eng.* **59** 689–96
- [23] Chang Y-H Y, Wang K, Wu C, Chen Y, Zhang C and Wang B 2015 A facile method for integrating direct-write devices into three-dimensional printed parts *Smart Mater. Struct.* **24** 065008
- [24] Robinson C J, Stucker B, Lopes A J, Wicker R and Palmer A J 2006 Integration of direct-write (DW) and ultrasonic consolidation (UC) technologies to create advanced structures with embedded electrical circuitry *17th Solid Freeform Fabrication Symp.* pp 60–9
- [25] Siggard E J, Madhusoodanan A S, Stucker B E and Eames B 2006 Structurally embedded electrical systems using ultrasonic consolidation (UC) *Proc. of the 17th Solid Freeform Fabrication Symp.* pp 70–83
- [26] Li J, Monaghan T, Masurtschak S, Bourmias-Varotsis A, Friel R J and Harris R A 2015 Exploring the mechanical strength of additively manufactured metal structures with embedded electrical materials *Mater. Sci. Eng. A* **639** 474–81
- [27] Li J, Monaghan T, Bourmias-Varotsis A, Masurtschak S, Friel R J and Harris R A 2014 Exploring the mechanical performance and material structures of integrated electrical circuits within solid state metal additive manufacturing matrices *Proc. of the 2014 Annual Solid Freeform Fabrication Symp.* pp 3–5

- [28] Johander P, Haasl S, Persson K and Harrysson U 2007 Layer manufacturing as a generic tool for microsystem integration *4M2007 Conf. Proc.* pp 1–4
- [29] Gibson I, Rosen D W and Stucker B 2010 *Additive Manufacturing Technologies: RAPID Prototyping to Direct Digital Manufacturing* (New York: Springer)
- [30] Choi J W, Wicker R, Lee S H, Choi K H, Ha C S and Chung I 2009 Fabrication of 3D biocompatible/biodegradable micro-scaffolds using dynamic mask projection microstereolithography *J. Mater. Process. Technol.* **209** 5494–503
- [31] Folgar C E, Folgar L N, Cormier D and Hill R 2013 Multifunctional material direct printing for laser sintering systems *Proc. of the 2013 Annual Int. Solid Freeform Fabrication Symp.* pp 282–96
- [32] MacDonald E, Salas R, Espalin D, Perez M, Aguilera E, Muse D and Wicker R B 2014 3D printing for the rapid prototyping of structural electronics *IEEE Access* **2** 234–42
- [33] Thompson J, Braddom E, Farris J and Mezenner R 2008 Digital projection of UV light for direct imaging applications, DLP technology is enabling the next generation of maskless lithography *Report* (http://focus.ti.com/pdfs/dlpdmd/Digital_Projection_of_UV_Light_is_Enabling_New_Markets1.pdf)
- [34] Zhang X, Wu D M, Sun C and Fang N 2005 Projection microstereolithography using digital micro-mirror dynamic mask *Sensors Actuators A* **121** 113–20
- [35] Choi J W, Ha Y M, Lee S H and Choi K-H 2006 Design of microstereolithography system based on dynamic image projection for fabrication of three-dimensional microstructures *J. Mech. Sci. Technol.* **20** 2094–104
- [36] Zhou C, Chen Y, Yang Z and Khoshnevis B 2013 Digital material fabrication using mask-image-projection-based stereolithography *Rapid Prototyping J.* **19** 153–65
- [37] Hon K K B, Li L and Hutchings I M 2008 Direct writing technology—advances and developments *CIRP Ann. Manuf. Technol.* **57** 601–20
- [38] Li B, Clark P A and Church K H 2007 Robust direct-write dispensing tool and solutions for micro/meso-scale manufacturing and packaging *Proc. of ASME 2007 Int. Manufacturing Science and Engineering Conf. (ASME)* pp 715–21
- [39] Epoxy Technology 2014 EPO-TEK® EJ2189 *Technical Data Sheet*
- [40] Epoxy Technology 2012 EPO-TEK® E4110-PFC *Technical Data Sheet*
- [41] Fischler M A and Bolles R C 1981 Random sample consensus: a paradigm for model fitting with applications to image analysis and automated cartography *Commun. ACM* **24** 381–95
- [42] Pandiri S 1987 The behavior of silver flakes in conductive epoxy adhesives *Adhes. Age* **30** 31–5